Earth and Planetary Science Letters 432 (2015) 332–341

Contents lists available at ScienceDirect

Earth and Planetary Science Letters

www.elsevier.com/locate/epsl

Estimates of olivine–basaltic melt electrical conductivity using a digital rock physics approach

Kevin J. Miller *,[1], Laurent G.J. Montési, Wen-lu Zhu

Department of Geology, University of Maryland at College Park, 8000 Regents Dr., College Park, MD 20742, United States

ARTICLE INFO

Article history:
Received 22 June 2015
Received in revised form 27 September 2015
Accepted 2 October 2015
Available online xxxx
Editor: B. Buffett

Keywords:
electrical conductivity
permeability
mid-ocean ridge
digital rock physics
melt fraction
olivine

ABSTRACT

Estimates of melt content beneath fast-spreading mid-ocean ridges inferred from magnetotelluric tomography (MT) vary between 0.01 and 0.10. Much of this variation may stem from a lack of understanding of how the grain-scale melt geometry influences the bulk electrical conductivity of a partially molten rock, especially at low melt fraction. We compute bulk electrical conductivity of olivine–basalt aggregates over 0.02 to 0.20 melt fraction by simulating electric current in experimentally obtained partially molten geometries. Olivine–basalt aggregates were synthesized by hot-pressing San Carlos olivine and high-alumina basalt in a solid–medium piston-cylinder apparatus. Run conditions for experimental charges were 1.5 GPa and 1350 °C. Upon completion, charges were quenched and cored. Samples were imaged using synchrotron X-ray micro-computed tomography (μ-CT). The resulting high-resolution, 3-dimensional (3-D) image of the melt distribution constitutes a digital rock sample, on which numerical simulations were conducted to estimate material properties. To compute bulk electrical conductivity, we simulated a direct current measurement by solving the current continuity equation, assuming electrical conductivities for olivine and melt. An application of Ohm's Law yields the bulk electrical conductivity of the partially molten region. The bulk electrical conductivity values for nominally dry materials follow a power-law relationship $\sigma_{\text{bulk}} = C\sigma_{\text{melt}}\phi^m$ with fit parameters $m = 1.3 \pm 0.3$ and $C = 0.66 \pm 0.06$. Laminar fluid flow simulations were conducted on the same partially molten geometries to obtain permeability, and the respective pathways for electrical current and fluid flow over the same melt geometry were compared. Our results indicate that the pathways for flow fluid are different from those for electric current. Electrical tortuosity is lower than fluid flow tortuosity. The simulation results are compared to existing experimental data, and the potential influence of volatiles and melt films on electrical conductivity of partially molten rocks is discussed.

1. Introduction

At mid-ocean ridges, melt is thought to percolate over a broad, partially molten region through a grain-scale network of interconnected melt (Fig. 1). The capacity of the upper mantle to transport melt, which is ultimately responsible for the production of oceanic crust, strongly depends on the spatial distribution of melt in the upper mantle. The magnetotelluric (MT) method, which exploits the high conductivity of partially molten rock, is a valuable tool used to probe the melt content of the upper mantle. Though MT measurements are consistent with the presence of partial melt at mid-ocean ridges, they disagree on the shape of the melting region and on the local melt fraction, with estimates in the literature varying from as low as 0.01–0.03 (Evans et al., 1999) to as much as 0.10 (Key et al., 2013). Though much of this variation is likely due to the presence of melt anisotropy (e.g. Pommier et al., 2015a; Zhang et al., 2014; Caricchi et al., 2011 and references therein), which is typically not accounted for when transforming conductivity to melt fraction profiles, the first step towards reconciling MT survey estimates is to robustly link electrical conductivity of partially molten mantle rocks to the grain-scale morphology and interconnectivity of melt under hydrostatic stress. A microstructure-based approach to constraining electrical conductivity as a function of melt fraction will provide a baseline for extrapolating laboratory measurement to natural conditions and to assess the potential contributions of volatiles and melt anisotropy to bulk electrical conductivity.

Bulk electrical conductivity of partially molten rock strongly depends on interconnectivity of the highly conductive melt phase. For a monomineralic system, under hydrostatic melting conditions,

* Corresponding author.
E-mail address: kevjmill@stanford.edu (K.J. Miller).
[1] Now at Department of Geophysics, Stanford University, 397 Panama Mall, Stanford, CA 94305, United States.

http://dx.doi.org/10.1016/j.epsl.2015.10.004
0012-821X/

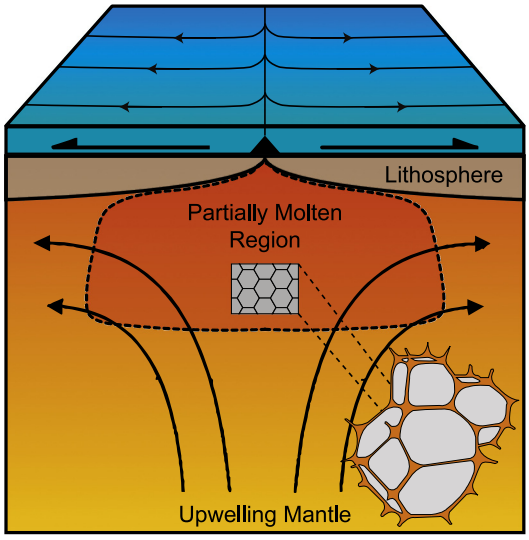

Fig. 1. Schematic diagram of a symmetrically spreading mid-ocean ridge. Surface arrows denote the spreading direction, curved arrows denote the upwelling direction of the mantle, blue region represents the ocean, brown represents the lithosphere, orange gradient represents the asthenosphere, and red represents the partially molten region beneath the ridge axis. Modified from Weatherley (2012). Pop-out figure is a depiction of an idealized, grain-scale melt geometry that is modified from Toramaru and Fujii (1986). (For interpretation of the references to color in this figure legend, the reader is referred to the web version of this article.)

melt settles into an equilibrium configuration that minimizes the total surface energy of the system (Fig. 1). The degree of interconnectivity can be assessed by the dihedral angle associated with its constituent solid–liquid phase boundaries (Bulau et al., 1979). For a dihedral angle greater than 60°, melt forms isolated pockets. In this case, the melt and solid phases are connected in series and the bulk electrical conductivity of the mixture is only marginally greater than that of the solid. However, for a dihedral angle less than 60°, as is the case for a partially molten olivine–basalt (Waff and Bulau, 1982), melt forms an interconnected network along grain edges (von Bargen and Waff, 1986). In this configuration, the melt conducts electricity in parallel with olivine and the bulk electrical conductivity for melt fractions greater than 0.01 increases by at least one order of magnitude (Roberts and Tyburczy, 1999; ten Grotenhuis et al., 2005; Yoshino et al., 2010).

Since the electrical conductivity of rock strongly depends on the melt geometry, bulk conductivity versus melt fraction relationships have been derived for a number of idealized melt geometries, such as a Hashin–Shtrikman sphere pack. Though idealized geometries are useful for conceptualizing melt configurations, partially molten mantle rocks are heterogeneous and exhibit a range of melt features (e.g. Miller et al., 2014; Waff and Faul, 1992) depending on the melt fraction present. At melt fraction larger than ~0.01, melt mostly resides in triple junctions connected at four-grain junctions (Miller et al., 2014; Waff and Bulau, 1982; Zhu et al., 2011 and references therein) though melt films that wet two-grain boundaries have also been observed at low melt fraction (e.g. Cmíral et al., 1998; Faul et al., 1994). Melt pools exist with increasing frequency as melt fraction increases, leading to an increased degree of grain boundary wetting or spillover from triple junctions (e.g., Miller et al., 2014; Zhu et al., 2011). At melt fraction of 0.2, melt pools are the dominant feature of the melt network (Miller et al., 2014; Zhu et al., 2011). The coexistence of multiple geometries for a given melt fraction highlights the importance to consider realistic, three-dimensional (3-D) melt geometries when computing material properties like electrical conductivity.

Experiments conducted on partially molten olivine–basalts find that bulk electrical conductivity varies as a power law with melt fraction (i.e., Archie's Law):

$$\sigma_{\text{bulk}} = C\sigma_{\text{melt}}\phi^{m} \tag{1}$$

where σ_{bulk} is bulk conductivity, σ_{melt} is melt conductivity, and ϕ is melt fraction. C and m are empirical power law parameters that depend on the melt morphology and interconnectivity. Values $m = 0.89$ to 1.30 and $C = 0.73$ to 1.47 have been reported for olivine–basalt partial melts (Pommier et al., 2015b; Roberts and Tyburczy, 1999; ten Grotenhuis et al., 2005; Yoshino et al., 2010). Though experimentally assessing the bulk electrical conductivity of olivine aggregates is necessary for accurately interpreting EM data, empirical relationships alone do not provide much textural information about the partially molten rock.

Most studies (Roberts and Tyburczy, 1999; ten Grotenhuis et al., 2005; Yoshino et al., 2010) find that the data on partially molten samples overlap the upper Hashin–Shtrikman bound, which is intended to represent a loose pack of uniformly wetted spheres. We argue that this interpretation is inconsistent with microstructural observations of texturally equilibrated rocks. While experimental constraints on the electrical conductivity of partially molten rock as a function of melt fraction are essential to interpret MT data, a direct link between electrical properties and melt geometry is still missing.

In addition, the use of electrical conductivity to infer permeability of systems where direct permeability measurements could be challenging, such as partially molten rocks, has garnered significant interest. With the assumptions that pathways for both conductivity and permeability are linked to the microstructure of the rock, several studies have discussed the apparent formation factor, defined as the $\sigma_{\text{bulk}}/\sigma_{\text{melt}}$ and its relation to microstructure in various porous media (e.g. Avellaneda and Torquato, 1991; Johnson et al., 1986; Katz and Thompson, 1987). A self-consistent analysis of permeability and electrical conductivity using network (David, 1993) and laminar flow models on periodic pore spaces (e.g. Martys and Garboczi, 1992; Schwartz et al., 1993) conclude that these approaches produce comparable results in terms of extrapolating permeability from electrical conductivity. They may even work empirically to deduce fluid flow information from electromagnetic data. However, the physics of laminar flow and direct electric current – both the governing equations and boundary conditions – are different. For example, while highly conductive impurities on grain boundaries can significantly enhance bulk conductivity in polycrystalline olivine (Watson et al., 2010), they will not support fluid flow. Therefore, one should not expect that changes in the melt microstructure, in this case by means of changing the melt fraction, have the same effect on permeability as it does on electrical conductivity. With this in mind, it is important to assess whether a link between permeability and electrical conductivity is physically justified.

In this study, we compute the bulk electrical conductivity and permeability of digital rocks composed of olivine and basaltic melt with texture equilibrated at isostatic mantle pressure–temperature conditions. We digitized each sample using synchrotron-based X-ray micro-computed tomography (μ-CT) (Zhu et al., 2011). The resulting 3-D images constitute digital rocks, on which direct current and fluid flow simulations were conducted.

2. Methods

2.1. Sample preparation and imaging

The samples considered in this study are synthetic olivine–basalts aggregates representing partially molten rocks (Miller et al., 2014; Zhu et al., 2011). Experimental charges were prepared from a powered mixture of Fo_{90} San Carlos olivine and natural, high-alumina basalt (Mg # = 0.0705) mixed in proportion to achieve

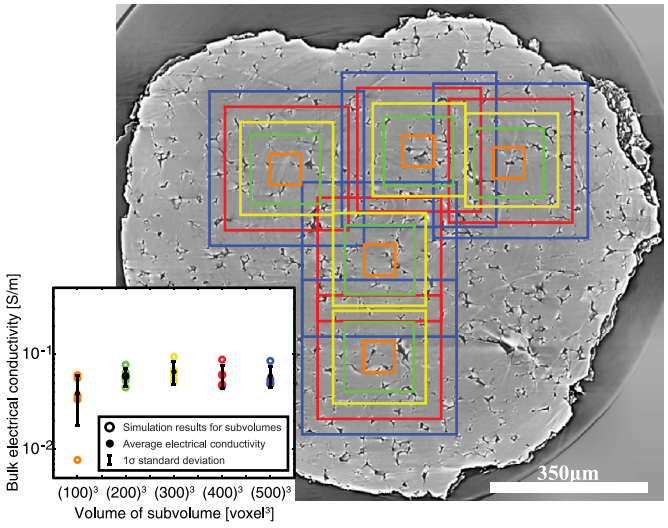

Fig. 2. Determination of a representative subvolume. Background is a cross-sectional tomography slice of a sample containing melt fraction 0.05. Slice was sampled along the radial–azimuthal plane of the cylindrical sample. Cubic subvolumes of various sizes were cropped from the sample and their bulk conductivities were computed, assuming olivine is a perfect insulator, and plotted as a function of volume (foreground). All subsequent computations were conducted on subvolume $400 \times 400 \times 400$ voxel^3 (280 μm)^3.

nominal melt fractions 0.02, 0.05, 0.10, and 0.20. Powdered mixtures were placed in graphite capsules. Charges were isostatically hot-pressed under simulated mantle pressure–temperature conditions (1.5 GPa and 1350 °C) in a solid–medium piston-cylinder apparatus for a minimum of 1 week to achieve textural equilibrium. Upon completion, charges were quenched, turning the molten basalt to glass, and ∼1 mm cores were drilled from the quenched aggregates. Cores were imaged using a combination of absorption-contrast and phase-contrast X-ray μ-CT at 27 keV to resolve the small density contrast between olivine and basaltic glass. Projections of the integrated X-ray absorption and phase shift were recorded over 180° at 0.12° increments and reconstructed into 3-D grayscale datasets. Detailed information on reconstruction procedure and image processing tools can be found in Miller et al. (2014). Voxel (3-D pixel) values in the reconstructed images roughly correspond to material density. Cubic voxels are 700 nm in length, measured along the voxel edge.

2.2. Subvolume selection

Samples often exhibit significant decompression cracking. These cracks are voids that are not present at elevated pressure and temperature. In order to avoid decompression cracks and reduce the size of the computational domain, we consider smaller subsets, or subvolumes, that are cropped from the full 3-D image datasets of whole samples (Miller et al., 2014). All the subvolumes used in direct current simulations, with the exception of those we used to assess the potential influence of H_2O, have dimensions 280 μm × 280 μm × 280 μm, which was determined to be representative of the bulk based on an electrical conductivity convergence analysis conducted on progressively larger, nested subvolumes (Fig. 2). At least three statistically representative subvolumes were cropped from each sample.

2.3. Noise-removal and segmentation

Grayscale subvolumes were processed according to the procedure detailed in Miller et al. (2014) to remove noise and artifacts, improving the efficacy of automatic segmentation algorithms. In order to setup a numerical domain for computation, grayscale subvolume data were transformed into label images using a variety of semi-automatic segmentation techniques, all of which are explained in detail in Miller et al. (2014).

The melt fraction of each subvolume was calculated by counting the number of cubic, uniform voxels labeled as basalt. A robust uncertainty analysis of the measured melt fraction requires access to the point-spread function of the image data, which is difficult to obtain. As an alternative, following Fusseis et al. (2012), we estimate lower and upper bounds for the melt fraction by measuring the melt fraction associated with the eroded and dilated melt image, respectively. Contractions and dilations were conducted along all three orthogonal directions of the cubic subvolume.

2.4. Direct current simulations

Though the electrical response of a partially molten rock is controlled by the variable mobility of charge carriers in response to an alternating electric field – either by ambient electromagnetic waves in the Earth or an alternating current source in the laboratory – we chose to simulate direct current to obtain bulk electrical conductivity. Despite this different approach, bulk electrical conductivity should not depend on the type of electrical source, whether it is inferred from the frequency-dependence of alternating current measurements or the direct current simulations. We focus on modeling charge transport by solving the current continuity equation and do not explicitly consider the mobility of charge carriers.

Our model is based on the formulations proposed by Garboczi (1998) and Zhan et al. (2010). Each segmented label image is the computational domain in a direct current simulation. We solve the current continuity equation, which is the Laplace equation

$$\nabla \cdot (\sigma \nabla \psi) = 0 \tag{2}$$

where σ is the local electrical conductivity [S m^{-1}] of voxels associated with each conductive material and ψ is the local scalar electric potential [V] defined at voxel centers. Electric current is driven by an imposed electric potential differential ($\Delta\Psi$) across the subvolume, between the inlet and outlet faces. A no-flux condition is imposed at the four faces parallel to the global electric potential gradient to ensure current is conserved (Fig. 3). Using a second-order centered finite-difference formulation, Eq. (2) at each voxel becomes

$$\sum_{j=1}^{n} \kappa_{ij}(\psi_j - \psi_i) = 0 \tag{3}$$

where n is the number of connecting voxels and κ_{ij} is the electrical conductance of the bond connecting voxels i and j. The distinction between electrical conductance and electrical conductivity is a geometric factor, which is unity for bonds connecting voxels in a uniform cubic grid. Voxels i and j are restricted to adjoining elements.

With consideration of the no-flux and inlet/outlet conditions, Eq. (3) is reformulated into a matrix equation

$$\kappa_{lm}\psi_m = b_l \tag{4}$$

where b_l is a vector that contains the influence of the boundary conditions on interior voxels and κ_{lm} is a positive definite, symmetric matrix that contains the electrical conductances of the bonds connecting each voxel. Elements are summed over m indices. An additional constraint on the system comes from current continuity, which states that the conductance of each bond must satisfy

$$\kappa_{lm} = \frac{2\sigma_l\sigma_m}{\sigma_l + \sigma_m} \tag{5}$$

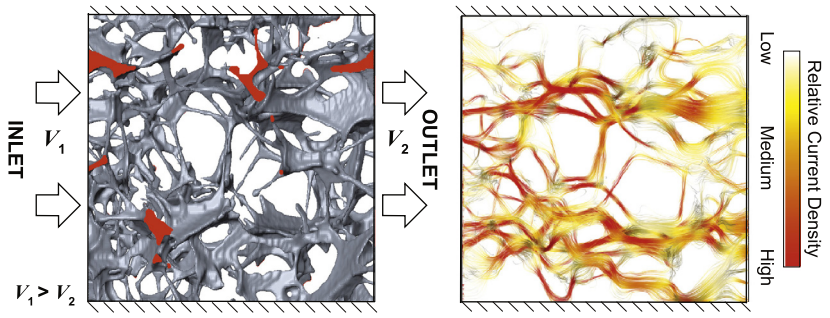

Fig. 3. Configuration of a numerical direct current experiment conducted along the x-axis of a $140 \times 140 \times 140$ μm^3 subvolume that contains 5 vol.% melt. (Left) Grey features are melt. Empty space represents solid grains. Red features denote the intersection of the melt with the bounding box. Arrows represent the flow direction of electric current across the model as a whole, driven by the difference is electric potential V_1 on the inlet side and V_2 on the outlet side. Hash marks illustrate the no-flux condition imposed on the intersections of the bounding box and material interface. (Right) Current density field is displayed as streamlines and color-coded according to the relative magnitude. Absolute magnitude is not important for visualization. In this simulation, olivine is considered a perfect insulator. (For interpretation of the references to color in this figure legend, the reader is referred to the web version of this article.)

If voxels l and m belong to the same material, the conductance of the connecting bond has the same values as the electrical conductivity of that material. Conductance between voxels that are not neighbors equals zero. Eq. (4) is solved using the conjugate gradient method to a tolerance of 1×10^{-5}. An incomplete Cholesky factorization (Meijerink and van der Vorst, 1977) was used as a preconditioner to improve convergence rate of the conjugate gradient solver. Each simulation was set-up, discretized, and solved using Matlab-based finite-difference software called Finite-difference electrical conductivity calculator (FDECC), which we built in-house.

The bulk electrical conductivity was calculated by computing the electric field, volume-averaging the z-component of the current density field, and applying Ohm's Law

$$J_z = -\sigma_{\text{bulk}} \frac{\Delta \Psi}{L} \tag{6}$$

where J_z is the current density averaged over the whole domain and L is the length of the subvolume in the direction parallel to the imposed electric potential gradient.

Evaluating the effect of melt films along grain boundaries requires a special procedure since the resolution of μ-CT is not sufficient to observe possible nanometer scale melt films. We employ an upper bound approach. First we use Avizo's *Separate Objects* module, based on the morphological watershed transform, to define likely olivine–olivine grain boundaries. Assuming all the interfaces are covered by melt films, each voxel at grain boundaries thus consists of both olivine and melt. We assign to these voxels an electrical conductivity that is the parallel average of the olivine and basalt conductivities,

$$\sigma_{\text{film}} = \sigma_{\text{melt}} \chi + \sigma_{\text{olivine}} (1 - \chi) \tag{7}$$

where χ is the proportion of the voxel that is occupied by melt. Assuming a melt films thickness of 100 nm, the maximum value reported in Cmíral et al. (1998), and considering that our voxels have a uniform thickness of the 700 nm, $\chi = 1/7$. This approach is the same used by Zhan et al. (2010) to model the effect of an electric double layer on bulk electrical conductivity of sandstone. This approach overestimates the effects of melt films along olivine–olivine grain boundary as the effective conductivity of the voxels should be anisotropic and Eq. (6) should only be valid in the grain-parallel direction. We are able to bracket the effect of the melt films by comparing simulations with $\chi = 0$ and $\chi = 1/7$.

2.5. Fluid flow simulations

Permeability simulations were conducted using Avizo XLab Hydro following Miller et al. (2014). In these simulations, accommodation zones, where fluid spreads evenly over the inlet and outlet faces, were appended to the sample subvolumes. The Stokes equations for viscous fluids, which assume steady-state laminar flow, were solved on a staggered finite-volume grid (see Miller et al., 2014 and references therein). Flow was induced by imposing pressure drop ΔP across the input and output faces. A no-flux condition was imposed at the olivine–melt interface and the intersection of the melt geometry with the bounding box. As XLab Hydro cannot take into account variations in material properties, we could not evaluate the effects of melt films using similar strategy as in the direct current simulations. Instead, we assigned a 1-voxel thick surface along the olivine–olivine boundaries as melt. This approach grossly exaggerates the effect of melt films on permeability, which in reality are no more than 1/7 voxel thick. The only alternative approach would have been to resample the melt geometry to a voxel size that is comparable to the actual melt film thickness (tens of nanometers). However, this approach would increase the number of degrees of freedom in our system to an unmanageable computational size, and as shown later, the exaggerated melt films, as handled by our simplified approach, alter both the permeability and the porosity in the simulations, with negligible effect on the porosity–permeability relationship of partially molten rocks.

2.6. Computing tortuosity

Since we solve for the velocity and electrical fields, it is straightforward to compute the tortuosity of each simulation. Tortuosity is defined as the ratio of length of the path a parcel of fluid – or electric current for direct current simulations – would travel through the geometry to the length of that geometry in the direction parallel to flow. To a good approximation, the tortuosity is given by

$$\tau = \frac{\langle u_{\text{mag}} \rangle}{\langle u_z \rangle} \tag{8}$$

(Duda et al., 2011) where u_{mag} is the velocity magnitude and u_z is the z-component of the velocity, assuming z is the direction of flow.

3. Results

3.1. Electrical conductivity

Bulk electrical conductivity was computed for each subvolume label image (280 μm)^3, assuming conductivities of 7.53 S m^{-1} (ten Grotenhuis et al., 2005) and 0.009 S m^{-1} (Constable, 2006) for nominally dry melt and olivine. Electrical conductivities were measured at 1475 °C in these experiments (ten Grotenhuis et al., 2005). Simulation results are reported as a function of the measured melt

Table 1
Direct current (using $\sigma_{melt} = 7.53\ S\,m^{-1}$ and $\sigma_{olivine} = 0.009\ S\,m^{-1}$) and fluid flow simulations results, including measured melt fractions, bulk electrical conductivity, and permeability.

Nominal melt fraction	Subvolume ID	Measured melt fraction, ϕ	σ_{bulk} [$S\,m^{-1}$]	Permeability, k [m^2]
0.2	2	0.1501 (−0.0285/ + 0.0297)	3.90×10^{-1}	1.45×10^{-13}
0.2	3	0.1980 (−0.0285/ + 0.0291)	5.25×10^{-1}	2.48×10^{-13}
0.2	4	0.1960 (−0.0296/ + 0.0302)	5.63×10^{-1}	2.85×10^{-13}
0.05	2	0.0539 (−0.0256/ + 0.0298)	1.01×10^{-1}	7.00×10^{-15}
0.05	3	0.0438 (−0.0212/ + 0.0255)	6.13×10^{-2}	4.02×10^{-15}
0.05	4	0.0439 (−0.0207/ + 0.0245)	6.30×10^{-2}	3.69×10^{-15}
0.05	5	0.0465 (−0.0221/ + 0.0261)	7.29×10^{-2}	4.25×10^{-15}
0.05	1	0.0562 (−0.0282/ + 0.0322)	1.05×10^{-1}	7.29×10^{-15}
0.2	1	0.1824 (−0.0296/ + 0.0305)	5.05×10^{-1}	2.47×10^{-13}
0.05	1	0.0485 (−0.0249/ + 0.0299)	7.50×10^{-2}	4.70×10^{-15}
0.1	2	0.0855 (−0.0267/ + 0.0289)	1.55×10^{-1}	2.15×10^{-14}
0.1	3	0.0845 (−0.0256/ + 0.0277)	1.62×10^{-1}	2.32×10^{-14}
0.1	4	0.0770 (−0.0244/ + 0.0266)	1.29×10^{-1}	1.56×10^{-14}
0.02	2	0.0164 (−0.009/ + 0.0111)	1.47×10^{-2}	3.24×10^{-16}
0.02	3	0.0140 (−0.0077/ + 0.0097)	1.35×10^{-2}	N/A
0.02	4	0.0115 (−0.0061/ + 0.0076)	1.38×10^{-2}	N/A
0.2	5	0.1986 (−0.0296/ + 0.0302)	5.69×10^{-1}	2.66×10^{-13}

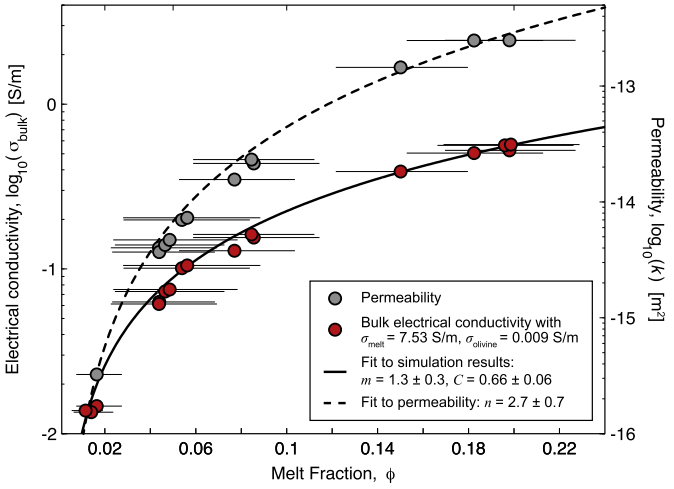

Fig. 4. Relations between electrical conductivity, permeability, and melt fraction reported on a log-linear scale. Results are fitted to Archie power-law relations. Permeabilities are fitted to power laws $k = C\phi^n$, where C and n are fit parameters.

fraction (Fig. 4). Each data point represents a computation on a single subvolume. Following experimental studies of olivine–basalt electrical conductivity, we logarithmically transform our electrical conductivity and melt fraction data and perform a linear fit of Archie's Law to our data (see Table 1). We obtain fit parameters $m = 1.3 \pm 0.3$ and $C = 0.66 \pm 0.6$, where m, often called the cementation exponent, takes into account the interconnectivity of the melt network and C is a scaling constant. At very low melt fraction, our fit using the conventional Archie's Law dips below the series mixing bound (discussed later in Section 4.3).

3.2. Permeability

Laminar flow simulations were conducted on the same subvolumes as the direct current simulations. Permeability is plotted as a function of melt fraction and compared to bulk electrical conductivity (Fig. 4). A fit to the permeability data in log–log space gives power law exponent $n = 2.7 \pm 0.7$, consistent with Miller et al. (2014). There is a clear difference in the power law curves between electrical conductivity and permeability as well as a difference in their respective pathways taken by electrical current and fluid. Fig. 5 shows that electricity flows more uniformly through the pore network and is less sensitive to relative frequency of pore diameters than fluid flow, which is consistent with the results of David (1993) and Martys and Garboczi (1992). Fluid flow, on the other hand, is dominated by a few major flow pathways through which most of the mass is transported.

3.3. Tortuosity

The tortuosity of our Stokes flow simulations, as computed by Eq. (5) (Fig. 6), is consistently higher than direct current simulations, which provides quantitative evidence that electricity flows diffusively through the entire melt network, whereas fluid flow focuses along specific pathways. It should be noted that the high tortuosity of direct current and fluid flow simulations conducted at $\phi = 0.02$ relative to those pertaining to higher melt fractions are likely due to low interconnectivity of the digital geometries at 2 vol.% melt, which may be artificially introduced by the resolution limitations of our imaging device. Since fluid travels through distinctly different pathways through the melt network than does electricity, generalization of empirical relations that link permeability and electrical conductivity lacks a microstructural justification, and should be verified case-by-case.

4. Discussion

4.1. Electrical conductivity and permeability comparison

Differences between the permeability and electrical conductivity of an aggregate can be attributed to the differences in the radius dependence between the fluid and electric fluxes. Consider a simple network of interconnected tubes of various widths. For each tube, there is an analytical expression for the fluid and electric fluxes. The fluid flux (Q) is given by

$$Q = \frac{\pi R^4}{8\mu}\frac{\Delta P}{L} \tag{9}$$

where R is the radius of the tube, μ is the viscosity of the fluid, ΔP is the pressure difference from one end of the tube to the other, and L is the tube length. The electric flux (Φ) is given by

$$\Phi = \pi R^2 \frac{\Delta \Psi}{L} \tag{10}$$

where $\Delta\Psi$ is the difference in electric potential from one end of the tube to the other. The strong dependence of the fluid flux on the radius of the tube causes fluid flow to be far more sensitive to the pathways available to flow. Since mass and current are both

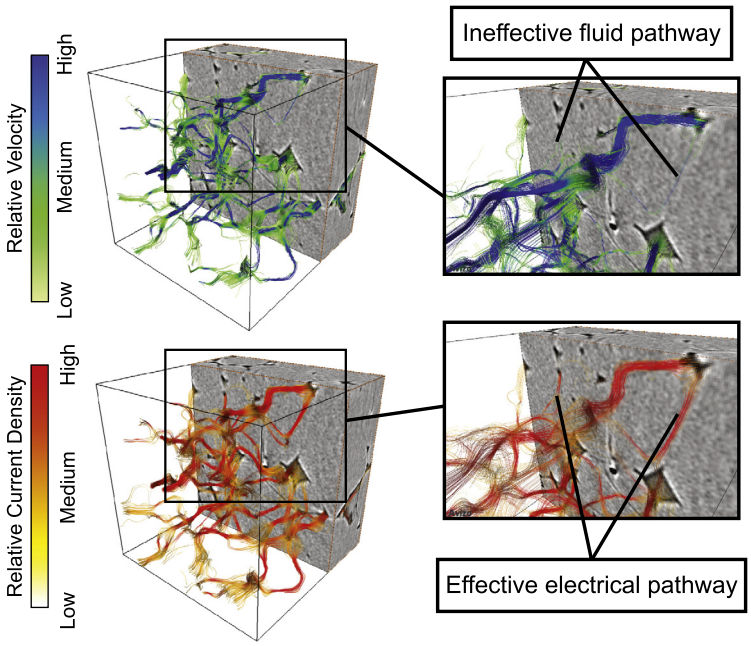

Fig. 5. Visual comparison of fluid flow (top) and direct current (bottom) simulation results. Streamlines are computed for the velocity (fluid flow) and current density (direct current) fields from randomly placed in space occupied by melt. Streamline seeds were randomly chosen – though weighted according to the magnitude of the field quantity – to emphasize locations of high magnitude. Seeds used for visualization of velocity streamlines are the same used for current density. (For interpretation of the colors in this figure, the reader is referred to the web version of this article.)

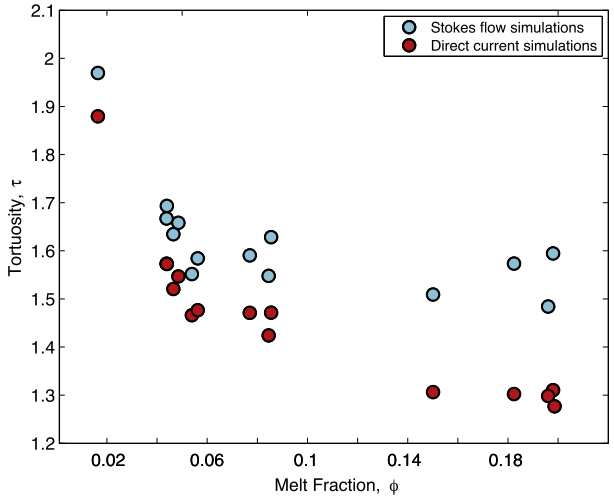

Fig. 6. Comparison of tortuosity for fluid flow and direct current simulations. Olivine is assumed to be a perfect insulator by imposing a no-flux condition on the olivine–melt interface, so electricity is conducting through only melt.

conserved quantities, the strong radius dependence of fluid flux results in the formation of a so-called "critical pathway" (David, 1993) through which most of the material is transported. The fact that tortuosity for laminar flow simulations is consistently higher than direct current simulations is evidence of these critical pathways.

4.2. Comparison with experimental data

Our simulation results on electrical conductivity are compared to mixing models (Fig. 7A) that assume idealized melt geometries and electrical conductivities for each material. Five different idealized melt geometries are considered: parallel and series bounds, upper and lower Hashin–Shtrikman bounds, and a geometric average model. The parallel composite model, which assumes melt is organized into a series of pipes that extend, with zero tortuosity, through an insulating secondary phase, constitutes an absolute upper bound for the bulk electrical conductivity. The series model is the parallel model rotated 90°, so that current must pass through both olivine and melt. It is the absolute lower bound for the bulk electrical conductivity of a composite material. Hashin–Shtrikman bounds are conceptually similar to the parallel and series bounds, except they assume a system composed of loosely packed spheres surrounded by a uniform layer of melt. The geometric mean model (Madden, 1976) considers a larger composite that consists of series and parallel sub-composites.

A fit to our simulation results using the conventional Archie's Law yields power law parameters $m = 1.3 \pm 0.3$ and $C = 0.66 \pm 0.06$, which is between the Hashin–Shtrikman bounds, assuming $\sigma_{\text{olivine}} = 0.009\ \text{S m}^{-1}$ and $\sigma_{\text{melt}} = 7.53\ \text{S m}^{-1}$. This is consistent with a heterogeneous melt distribution like that observed in microscopy studies (e.g. Cmíral et al., 1998; Garapić et al., 2013; Miller et al., 2014). Our results are systematically offset from the Hashin–Shtrikman upper boundary by a factor of 2 to 3, which is inconsistent with experimentally measured partially molten olivine–basalt electrical conductivities that often shown to overlap with the upper Hashin–Shtrikman bound (ten Grotenhuis et al., 2005; Yoshino et al., 2010). Although we do not have access to the actual samples from these studies, the chemistry, mineralogy, and preparation procedures are nominally the same as our own, suggesting that there is an additional contribution to the bulk conductivity that cannot be accounted for by separately considering the electrical conductivity of olivine and melt. A self-consistent study in which digital rock physics simulations are supplemented by impedance spectroscopy of the same samples, similar to Watson and Roberts (2011), would be immensely valuable to the field.

Recently, Zhang et al. (2014) measured the electrical conductivity of sheared partially molten peridotite. They separately measured the electrical conductivity of their melt and partially molten aggregates before and after deformation and found the electrical conductivity of their undeformed aggregate to be between the Hashin–Shtrikman lower and upper bounds, consistent with our

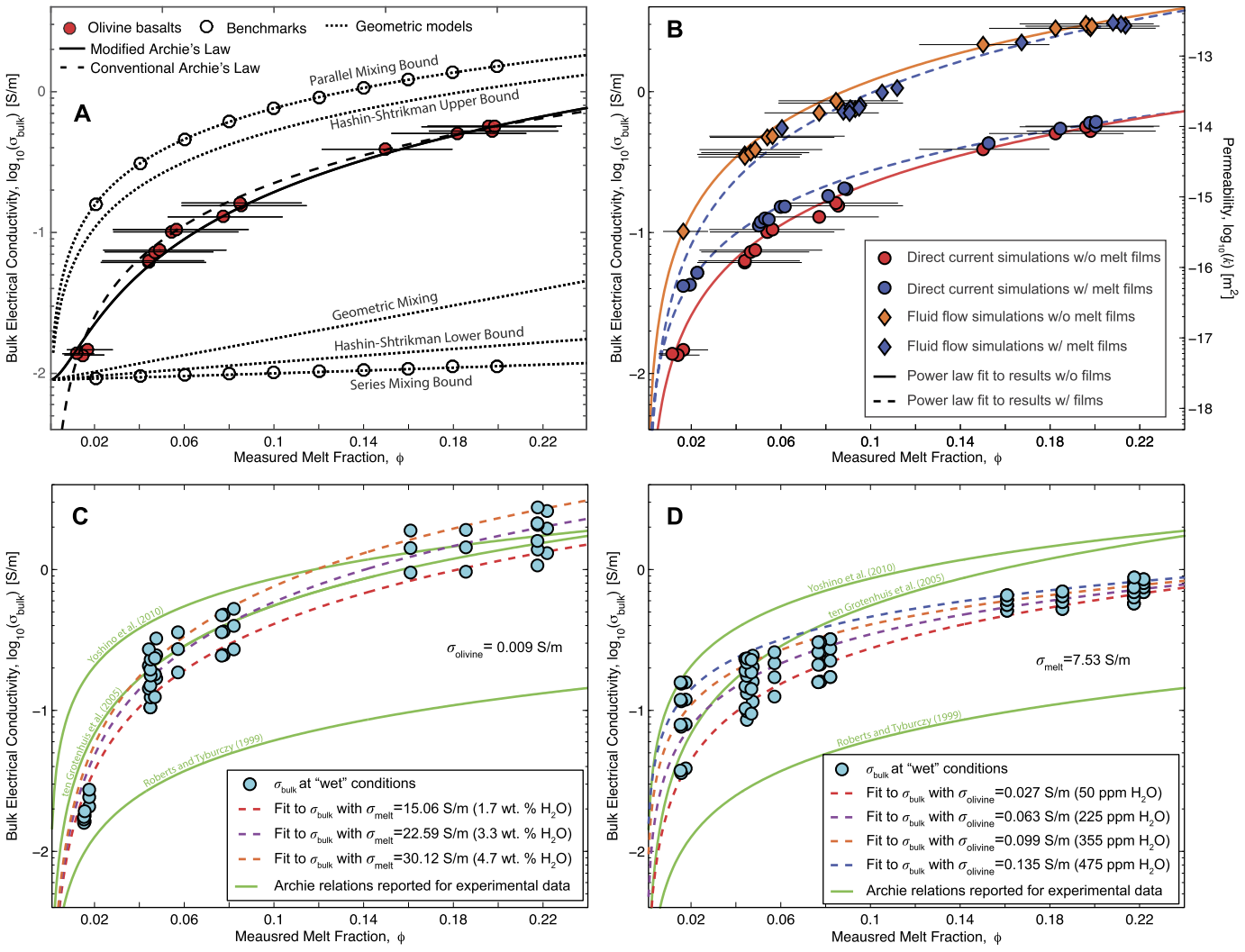

Fig. 7. A) Comparison of bulk electrical conductivity computed from partially molten geometries obtain from μ-CT and mixing models for idealized melt geometries. Direct current simulations are conducted on synthetic datasets for straight tubes and serial layers for parallel and series bounds, respectively, to demonstrate the accuracy of the numerical model. Two different equations were used to fit the electrical conductivity data: conventional Archie's Law (dotted line) and the modified Archie's Law (solid line). B) Influence of melt films on bulk electrical conductivity and permeability computed using the three-phase conductivity model. C) Influence of H_2O in melt on the bulk electrical conductivity and comparison with experimental data. Smaller $140 \times 140 \times 140$ μm^3 were used for computation. D) Influence of H_2O in olivine on the bulk electrical conductivity and comparison with experimental data. Smaller $140 \times 140 \times 140$ μm^3 were used for computation.

study. Though they interpret their measured value to the presence of high surface energy phases, which may reduce interconnectivity of the melt network. The electrical conductivity of the deformed sample, measured in the shear direction, overlapped the parallel mixing bound (i.e. electrical conduction through parallel pipes), which is consistent with deformation-induced melt segregation (Holtzman et al., 2003).

Our study provides a rigorous link between melt distribution geometry and electrical conductivity. Direct current simulations on synthetic datasets of straight and parallel tubes are in good agreement with analytical solutions to the Laplace equation. Due to limitations in current imaging techniques, it is conceivable that some connections of the melt network are missing from the melt distribution obtained for samples with low melt fractions. However, the missing connections could not explain the discrepancy between our simulation results and the experimental data because simulations conducted on subvolumes containing nominal melt fractions 0.10 and 0.20, in which melt channels are completely interconnected, still yield electrical conductivity values less than experimental measurements. However, melt films, which are too thin to resolve with μ-CT, and the presence of H_2O in melt and olivine during electrical conductivity measurements, may play an important role. We describe below what the effect of these features would be.

4.3. Modified Archie's Law

The benefit of Archie's Law over other geometric mixing laws is that the interconnectivity of the pore network is accounted for in the cementation exponent m. However, a fit of the conventional Archie's Law to our electrical conductivity data (Fig. 7A) produces a curve that dips below the series mixing bound for very low melt faction. Glover et al. (2000) showed that the geometric parameter C in the Archie's Law is not a constant for a partially molten rock, as it is a function of melt fraction. They suggested that the bulk electrical conductivity of a partially molten olivine–basalt aggregate could be better modeled by a linear combination of two power laws: one for melt and the other for olivine,

$$\sigma_{\text{bulk}} = \sigma_{\text{melt}}\phi^{r} + \sigma_{\text{olivine}}(1-\phi)^{p} \tag{11}$$

Like m in the conventional Archie's Law, r is an empirical parameter that accounts for the morphology and interconnectivity of the

melt phase, and p accounts for the interconnectivity of the olivine phase. Since the space occupied by olivine is the negative space occupied by the melt, p can be expressed as a function of r.

$$p = \frac{\log(1-\phi^r)}{\log(1-\phi)} \tag{12}$$

This modified Archie's Law is guaranteed to give a bulk electrical conductivity that is between the series and parallel mixing bounds. For completeness, we performed a fit of the modified Archie's Law to our data and obtained a value of $r = 1.6 \pm 0.3$. Results are plotted in Fig. 7A. The fit was performed using an orthogonal distance regression, which is part of OriginLab Pro statistical analysis software.

4.4. Melt films

In addition to melt tubules and pools, a number of high-resolution studies (e.g. Cmíral et al., 1998; Faul et al., 1994; Garapić et al., 2013) document thin films of melt at some two-grain junctions The thickness of melt films ranges between 3 nm and 100 nm. It has been suggested that thin films control melt transport at low melt fraction (Faul, 1997). We apply our direct current and Stokes flow models to quantifying the influence of melt films on bulk electrical conductivity and permeability using the approximations to melt films described in Section 2.4. By assuming all olivine–olivine boundaries are wetted by melt – the anisotropic electrical conductivity of grain boundaries that contain melt films is neglected – our approach gives an upper bound for the influence of melt films. Fluid flow simulations are conducted assuming that a full, 1 voxel fluid layer wets grain–grain boundaries.

Results are plotted in Fig. 7B. Artificially imposing melt films in our olivine–basalt geometry increases sample conductivity and has a similar effect on the bulk conductivity as increasing olivine electrical conductivity. This is because the voxels at grain boundaries are now considered an average of olivine and melt electrical conductivities, whereas these voxels were considered olivine only in the previous series of simulations. Bulk electrical conductivity increases substantially at low melt fraction and less so for higher melt fraction. The large error bounds on our melt fraction suggest that this change for $\phi > 0.02$ is within uncertainty. Nevertheless, the inclusion of melt films alone cannot account for the high electrical conductivities observed in experiments, even though their effect is grossly exaggerated in our simulations.

Including melt films substantially increases the permeability of our partial melt geometries. At the same time, the presence of melt films also substantially increase melt fraction. Recall that the melt films are grossly exaggerated in the permeability calculation. The resulting porosity–permeability relationship does not differ significantly from that of Miller et al. (2014) without melt films. Actually, the permeability of a subvolume that includes melt films is systematically lower that permeability of a subvolume of similar porosity but that does not include melt films. Although the difference is minimal and likely insignificant, melt films reduce permeability for a given porosity.

The larger effect of the melt films on bulk electrical conductivity relative to permeability is consistent with the concept of a critical pathway. In permeability computations, melt films contribute little to the critical pathways because the strong dependence of fluid flux on hydraulic radius renders melt films extremely ineffective fluid pathways, and melt primarily transport through triple junctions. In contrast, electrical conductivity flows more diffusively and uses melt films as viable pathways for electric transport. Thus melt films may be important contributors to the electrical properties of partially molten rocks at low melt fraction, especially if their chemistry is distinct from chemistry of the melt (Wirth, 1996). However, their contribution to the bulk electrical conductivity is not sufficient to account for the apparent discrepancy between the simulated and measured bulk electrical conductivities.

4.5. H_2O in melt

The presence of volatiles, specifically H_2O and CO_2, in melt is an excellent candidate for enhancing bulk electrical conductivity at high melt fraction. The addition of ~1 wt.% H_2O to an otherwise dry basaltic melt can increase the electrical conductivity by a factor of 3 (Ni et al., 2011). CO_2 has an even stronger effect on the melt electrical conductivity (Sifré et al., 2014; Yoshino et al., 2010) but is not explicitly addressed here. To assess the effect of H_2O on the bulk electrical conductivity of partial molten rocks, we run direct current simulations for various melt conductivities and convert to H_2O concentration for the melt using

$$\log\sigma_{\text{melt}} = 2.172 - \frac{860.82 - 204.46\sqrt{C_{H_2O}}}{T - 1146.8} \tag{13}$$

where C_{H_2O} is the concentration of H_2O in the melt and T is temperature (Ni et al., 2011). Though different degrees of melting will likely produce subsequently different H_2O concentrations – H_2O will partition from olivine to melt – we assume a uniform increase in the melt conductivity.

Our results are presented in Fig. 7C. A H_2O concentration of 1.7 wt.% is sufficient to explain the high conductivities for high melt fraction in ten Grotenhuis et al. (2005) but underestimates the conductivity at lower melt fraction. Therefore, the electrical conductivity–melt fraction power-law does not match their experimental results at lower melt fraction. As melt fraction decreases, the electrical conductivity of olivine will have a stronger influence on the bulk electrical conductivity.

4.6. H_2O in olivine

Under hot, "dry" conditions, the electrical conductivity of olivine, which is controlled by polaron electron hopping (e.g. Wanamaker and Duba, 1993; Yoshino et al., 2009 and references therein), is three to four orders of magnitude less than that of basaltic melt and should contribute insignificantly to the bulk electrical conductivity. Under "wet" conditions, however, olivine electrical conductivity can increase significantly (e.g. Dai and Karato, 2014; Wang et al., 2006; Yoshino et al., 2009 and references therein) though the magnitude of its influence on the bulk electrical conductivity of olivine is debated (Gardés et al., 2014).

To explore the effect of an increased olivine electrical conductivity due to the presence of H_2O, we run direct current simulations using a range of higher olivine conductivities. The conductivity of olivine with some fraction of water is estimated according to the model of Gardés et al. (2014). They consider three superposed conduction mechanisms. The first two, diffusion of cation vacancies and polaron hopping, dominate under anhydrous conditions at high and low temperatures, respectively (Gardés et al., 2014 and references therein), while the third mechanism is related to the presence of hydrogen in olivine.

$$\sigma = \sigma_0^{\text{vacancy}} e^{-\frac{\Delta H^{\text{vacancy}}}{RT}} + \sigma_0^{\text{polaron}} e^{-\frac{\Delta H^{\text{polaron}}}{RT}} + \sigma_0^{\text{hydrous}} C_{H_2O} e^{-\frac{\Delta H^{\text{hydrous}} - \alpha C_{H_2O}^{1/3}}{RT}} \tag{14}$$

where ΔH are the activation enthalpies for the mechanisms, C_{H_2O} is the weight concentration of H_2O in the olivine, α corrects for the decrease in the activation enthalpy for increasing H_2O concentration, R is the ideal gas constant, and T is temperature.

The simulation results are plotted in Fig. 7D. If the conductivities of melt and olivine are those stated in Fig. 7D, we find that increasing olivine conductivity noticeably enhances the bulk conductivity at low melt fraction and changes the shape of the bulk electrical conductivity–melt fraction power-law. If we assume wet conditions for both olivine and melt, we find that $\sigma_{melt} = 15.60$ S/m and $\sigma_{olivine} = 0.045$ S/m explains experimental data by ten Grotenhuis et al. (2005). An olivine electrical conductivity of 0.045 S/m at 1475 °C (temperature of ten Grotenhuis et al. (2005) experiments) translates to ∼145 ppm of water in olivine. Given that the solubility of H_2O in olivine is ∼90 ppm (Gaetani et al., 2014), measured at 1200 °C, it is difficult to justify 145 ppm H_2O concentration in olivine. However, without solubility data measured at higher melt temperature, it is unclear whether the solubility of H_2O in olivine at 1200 °C can be extrapolated to 1475 °C.

The trend of the data from laboratory measurements (e.g., ten Grotenhuis et al., 2005) may reflect water in the aggregates, with the combined effect of water in olivine and melt films dominant at low melt fraction and water in the melt dominant a high melt fraction. Neither effect is expected to significantly affect the relation between permeability and melt fraction.

4.7. Chemical heterogeneity

We speculate the existence of a thin, electrochemically distinct layer at the olivine–melt interface that might may account for the apparent discrepancy between the bulk electrical conductivities measured and those we computed using real partial melt geometries. Electrolytic conduction by Na^+ ions dissolved in the fluid is the primary mode of electrical transport in porous rhyolite (Gaillard, 2004). High concentration of Na^+ ions at the mineral–fluid interface would provide an addition pathway for electrical conduction. In crustal rocks, lattice deficiencies at the surface of clay minerals result in a locally negative charge that attracts ions in solution (Zhan et al., 2010), coating the mineral–fluid interface with a thin, highly conductive layer, often called the electric double layer (EDL). The thickness of the EDL is roughly the Debye length (Morgan et al., 1989), which depends on physical parameters of the fluid phase, such as the molarity and permittivity of solution. For reference, the Debye length of the clay–water interface is on the order of a few to tens of nanometers (Tombácz and Szekeres, 2006 and references therein). Though the thickness of the EDL is quite small compared to the diameter of the melt conduits, the local electrical conductivity of the EDL would be greater than that of the fluid, and since it forms an interconnected pathway, will conduct in parallel with the fluid. Therefore, electrical conduction near the mineral–fluid interface may be a separate and important conduction mechanism to consider, especially at low fluid fraction.

The existence of EDLs in partially molten olivine–basalts is currently not considered in literature, since the chemistry of olivine–melt interface is intrinsically different from the clay–water interface. The formation of an EDL on an olivine–melt interface would require a local charge imbalance, possibly due to concentration of impurities at the olivine–melt interface. Gurmani et al. (2011) and Wirth (1996) have proposed chemical variations in the presence of melt films but not for every olivine–melt interface. Nevertheless, the presence of EDLs – or more generally a spatial heterogeneity of the primary charge carriers – is a convenient mechanism to reconcile our model results and laboratory measurements. Furthermore, the influence of EDL on the bulk conductivity may be invisible to impedance spectroscopy if electrical conduction through EDLs operates in the same frequency spectrum as electrolytic conduction. Unfortunately, modeling the influence of the EDL on bulk conductivity requires a priori knowledge of the Debye length and EDL electrical conductivity, which to our knowledge have not been constrained for the partially molten olivine–basalt system.

5. Conclusion

We modeled direct current on experimentally obtained olivine–basalt partial melt geometries in order to link microstructural properties to bulk electrical conductivity and deconvolute the role of melt geometry from other processes, e.g. volatile content, that may affect electrical properties. Our digital rock physics approach for determining the bulk electrical conductivity of partially molten rocks has the benefit of having fine control on the physics and material properties of the system, while still adhering to a real melt geometry. Rather than having to rely on an idealized melt geometry from measured electrical properties of the system, we are able to compute electrical properties directly from the melt microstructure.

We found that the high bulk electrical conductivities observed in experiments cannot be accounted for by considering only a two-phase olivine–melt model unless there is significant enhancement of the melt electrical conductivity by volatiles. The trends observed in laboratory measurements may reflect water in the aggregates, with the combined effect of water in olivine and melt films dominant at low melt fraction, and water in the melt dominant at high melt fraction. Neither effect is expected to significantly affect the relation between permeability and melt fraction. We speculate that a high electrical conductivity, chemically distinct electrochemical layer on the grain–melt interface may also affect laboratory measurements. Such layers have been well characterized in rocks that contain clay minerals but have not been discussed in the context of partially molten mantle rocks.

Acknowledgements

This research used resources of the Advanced Photon Source, a U.S. Department of Energy (DOE) Office of Science User Facility operated for the DOE Office of Science by Argonne National Laboratory under Contract No. DE-AC02-06CH11357. This project is partially supported by National Science Foundation through Grant NSF-EAR1250338 and the Department of Energy through Grant DE-FG02-07ER15916. Support from the Ann G. Wylie Dissertation Fellowship is acknowledged.

We thank G. Gaetani and E. Sarafian from Woods Hole Oceanographic Institution (WHOI) for their insight regarding water content in mantle minerals and melts. We are very grateful to V. Le Roux, also from WHOI, who kindly provided us access to her computer for running direct current simulations on statistically representative subvolumes. We thank A. Pommier and an anonymous reviewer for their constructive reviews.

References

Avellaneda, M., Torquato, S., 1991. Rigorous link between fluid permeability, electrical conductivity, and relaxation times for transport in porous media. Phys. Fluids A, Fluid Dyn. 3, 2529. http://dx.doi.org/10.1063/1.858194.

Bulau, J.R., Waff, H.S., Tyburczy, J.A., 1979. Mechanical and thermodynamic constraints on fluid distribution in partial melts. J. Geophys. Res. 84, 6102–6108. http://dx.doi.org/10.1029/JB084iB11p06102.

Caricchi, L., Gaillard, F., Mecklenburgh, J., Le Trong, E., 2011. Experimental determination of electrical conductivity during deformation of melt-bearing olivine aggregates: implications for electrical anisotropy in the oceanic low velocity zone. Earth Planet. Sci. Lett. 302, 81–94. http://dx.doi.org/10.1016/j.epsl.2010.11.041.

Cmíral, M., Fitz, J.D., Faul, U.H., Green, D.H., 1998. A close look at dihedral angles and melt geometry in olivine–basalt aggregates: a TEM study. Contrib. Mineral. Petrol. 130, 336–345. http://dx.doi.org/10.1007/s004100050369.

Constable, S., 2006. SEO3: a new model of olivine electrical conductivity. Geophys. J. Int. 166, 435–437. http://dx.doi.org/10.1111/j.1365-246X.2006.03041.x.

Dai, L., Karato, S., 2014. The effect of pressure on the electrical conductivity of olivine under the hydrogen-rich conditions. Phys. Earth Planet. Inter. 232, 51–56.

David, C., 1993. Geometry of flow paths for fluid transport in rocks. J. Geophys. Res. 98, 12267. http://dx.doi.org/10.1029/93JB00522.

Duda, A., Koza, Z., Matyka, M., 2011. Hydraulic tortuosity in arbitrary porous media flow. Phys. Rev. E 84. http://dx.doi.org/10.1103/PhysRevE.84.036319.

Evans, R., Tarits, P., Chave, A., White, A., Heinson, G., Filloux, J., Toh, H., Seama, N., Utada, H., Booker, J., Unsworth, M., 1999. Asymmetric electrical structure in the mantle beneath the East Pacific Rise at 17°S. Science 286, 752–756. http://dx.doi.org/10.1126/science.286.5440.752.

Faul, U.H., 1997. Permeability of partially molten upper mantle rocks from experiments and percolation theory. J. Geophys. Res. 102, 10299–10311. http://dx.doi.org/10.1029/96JB03460.

Faul, U.H., Toomey, D.R., Waff, H.S., 1994. Intergranular basaltic melt is distributed in thin, elongated inclusions. Geophys. Res. Lett. 21, 29–32. http://dx.doi.org/10.1029/93GL03051.

Fusseis, F., Schrank, C., Liu, J., Karrech, A., Llana-Fúnez, S., Xiao, X., Regenauer-Lieb, K., 2012. Pore formation during dehydration of a polycrystalline gypsum sample observed and quantified in a time-series synchrotron X-ray micro-tomography experiment. Solid Earth 3, 71–86. http://dx.doi.org/10.5194/se-3-71-2012.

Gaetani, G.A., O'Leary, J.A., Koga, K.T., Hauri, E.H., Rose-Koga, E.F., Monteleone, B.D., 2014. Hydration of mantle olivine under variable water and oxygen fugacity conditions. Contrib. Mineral. Petrol. 167, 1–14. http://dx.doi.org/10.1007/s00410-014-0965-y.

Gaillard, F., 2004. Laboratory measurements of electrical conductivity of hydrous and dry silicic melts under pressure. Earth Planet. Sci. Lett. 218, 215–228. http://dx.doi.org/10.1016/S0012-821X(03)00639-3.

Garapić, G., Faul, U.H., Brisson, E., 2013. High-resolution imaging of the melt distribution in partially molten upper mantle rocks: evidence for wetted two-grain boundaries. Geochem. Geophys. Geosyst. 14, 1–11. http://dx.doi.org/10.1029/2012GC004547.

Garboczi, E.J., 1998. Finite Element and Finite Difference Programs for Computing the Linear Electric and Elastic Properties of Digital Images of Random Materials. Building and Fire Research Laboratory, National Institute of Standards and Technology.

Gardés, E., Gaillard, F., Tarits, P., 2014. Toward a unified hydrous olivine electrical conductivity law. Geochem. Geophys. Geosyst., 4984–5000. http://dx.doi.org/10.1002/2014GC005496.

Glover, P.W.J., Hole, M.J., Pous, J., 2000. A modified Archie's law for two conducting phases. Earth Planet. Sci. Lett. 180, 369–383.

Gurmani, S.F., Jahn, S., Brasse, H., Schilling, F.R., 2011. Atomic scale view on partially molten rocks: molecular dynamics simulations of melt-wetted olivine grain boundaries. J. Geophys. Res., Solid Earth 116, 1–9. http://dx.doi.org/10.1029/2011JB008519.

Holtzman, B.K., Kohlstedt, D.L., Zimmerman, M.E., Heidelback, F., Hiraga, T., Hustoftm, J., 2003. Melt segregation and strain partitioning: implications for seismic anisotropy and mantle flow. Science 301, 1227–1230. http://dx.doi.org/10.1126/science.1087132.

Johnson, D.L., Koplik, J., Schwartz, L.M., 1986. New pore-size parameter characterizing transport in porous media. Phys. Rev. Lett. 57, 2564–2567. http://dx.doi.org/10.1103/PhysRevLett.57.2564.

Katz, A.J., Thompson, A.H., 1987. Prediction of rock electrical conductivity from mercury injection measurements. J. Geophys. Res. 92, 599. http://dx.doi.org/10.1029/JB092iB01p00599.

Key, K., Constable, S., Liu, L., Pommier, A., 2013. Electrical image of passive mantle upwelling beneath the northern East Pacific Rise. Nature 495, 499–502. http://dx.doi.org/10.1038/nature11932.

Madden, T., 1976. Random networks and mixing laws. Geophysics 41, 1104–1125. http://dx.doi.org/10.1190/1.2035907.

Martys, N., Garboczi, E.J., 1992. Length scales relating the fluid permeability and electrical conductivity in random two-dimensional model porous media. Phys. Rev. B 46, 6080–6090. http://dx.doi.org/10.1103/PhysRevB.46.6080.

Meijerink, J.A., van der Vorst, H.A., 1977. An iterative solution method for linear systems of which the coefficient matrix is a symmetric M-matrix. Math. Comput. 31, 148. http://dx.doi.org/10.1090/S0025-5718-1977-0438681-4.

Miller, K.J., Zhu, W., Montési, L.G.J., Gaetani, G.A., 2014. Experimental quantification of permeability of partially molten mantle rock. Earth Planet. Sci. Lett. 388, 273–282. http://dx.doi.org/10.1016/j.epsl.2013.12.003.

Morgan, F.D., Williams, E.R., Madden, T.R., 1989. Streaming potential properties of westerly granite with applications. J. Geophys. Res. 94, 12449. http://dx.doi.org/10.1029/JB094iB09p12449.

Ni, H., Keppler, H., Behrens, H., 2011. Electrical conductivity of hydrous basaltic melts: implications for partial melting in the upper mantle. Contrib. Mineral. Petrol. 162, 637–650. http://dx.doi.org/10.1007/s00410-011-0617-4.

Pommier, A., Leinenweber, K., Kohlstedt, D.L., Qi, C., Garnero, E.J., Mackwell, S.J., Tyburczy, J.A., 2015a. Experimental constraints on the electrical anisotropy of the lithosphere–asthenosphere system. Nature 522, 202–206. http://dx.doi.org/10.1038/nature14502.

Pommier, A., Leinenweber, K., Tasaka, M., 2015b. Experimental investigation of the electrical behavior of olivine during partial melting under pressure and application to the lunar mantle. Earth Planet. Sci. Lett. 1. http://dx.doi.org/10.1016/j.epsl.2015.05.052.

Roberts, J.J., Tyburczy, J.A., 1999. Partial-melt electrical conductivity: influence of melt composition. J. Geophys. Res. 104, 7055. http://dx.doi.org/10.1029/1998JB900111.

Schwartz, L., Martys, N., Bentz, D., 1993. Cross-property relations and permeability estimation in model porous media. Phys. Rev. E 48, 4584–4591. http://dx.doi.org/10.1103/PhysRevE.48.4584.

Sifré, D., Gardés, E., Massuyeau, M., Hashim, L., Hier-Majumder, S., Gaillard, F., 2014. Electrical conductivity during incipient melting in the oceanic low-velocity zone. Nature 509, 81–85. http://dx.doi.org/10.1038/nature13245.

ten Grotenhuis, S.M., Drury, M.R., Spiers, C.J., Peach, C.J., 2005. Melt distribution in olivine rocks based on electrical conductivity measurements. J. Geophys. Res., Solid Earth 110, 1–11. http://dx.doi.org/10.1029/2004JB003462.

Tombácz, E., Szekeres, M., 2006. Surface charge heterogeneity of kaolinite in aqueous suspension in comparison with montmorillonite. Appl. Clay Sci. 34, 105–124. http://dx.doi.org/10.1016/j.clay.2006.05.009.

Toramaru, A., Fujii, N., 1986. Connectivity of melt phase in a partially molten peridotite. J. Geophys. Res. 91 (B9), 9239–9252. http://doi.org/10.1029/JB091iB09p09239.

von Bargen, N., Waff, H.S., 1986. Permeabilities, interfacial areas and curvatures of partially molten systems: results of numerical computations of equilibrium microstructures. J. Geophys. Res. 91, 9261–9276. http://dx.doi.org/10.1029/JB091iB09p09261.

Waff, H., Bulau, J., 1982. Experimental determination of near-equilibrium textures in partially molten silicates at high pressures. In: High Press. Res. Geophys., pp. 229–236.

Waff, H., Faul, U., 1992. Effects of crystalline anisotropy on fluid distribution in ultramafic partial melts. J. Geophys. Res. 97, 9003–9014. http://dx.doi.org/10.1029/92JB00066.

Wanamaker, B.J., Duba, A.G., 1993. Electrical conductivity of San Carlos olivine along [100] under oxygen – and pyroxene – buffered conditions and implications for defect equilibria. J. Geophys. Res., Solid Earth 98, 489–500. http://dx.doi.org/10.1029/92JB01584.

Wang, D., Mookherjee, M., Xu, Y., Karato, S., 2006. The effect of water on the electrical conductivity of olivine. Nature 443, 977–980. http://dx.doi.org/10.1038/nature05256.

Watson, H.C., Roberts, J.J., Tyburczy, J.A., 2010. Effect of conductive impurities on electrical conductivity in polycrystalline olivine. Geophys. Res. Lett. 37, 1–6. http://dx.doi.org/10.1029/2009GL041566.

Watson, H.C., Roberts, J.J., 2011. Connectivity of core forming melts: experimental constraints from electrical conductivity and X-ray tomography. Phys. Earth Planet. Inter. 186, 172–182.

Weatherley, S., 2012. Melting and Melt Migration in Heterogeneous Mantle Beneath Mid-ocean Ridges. University of Oxford.

Wirth, R., 1996. Thin amorphous films (1–2 nm) at olivine grain boundaries in mantle xenoliths from San Carlos, Arizona. Contrib. Mineral. Petrol. 124, 44–54. http://dx.doi.org/10.1007/s004100050172.

Yoshino, T., Laumonier, M., McIsaac, E., Katsura, T., 2010. Electrical conductivity of basaltic and carbonatite melt-bearing peridotites at high pressures: implications for melt distribution and melt fraction in the upper mantle. Earth Planet. Sci. Lett. 295, 593–602. http://dx.doi.org/10.1016/j.epsl.2010.04.050.

Yoshino, T., Matsuzaki, T., Shatskiy, A., Katsura, T., 2009. The effect of water on the electrical conductivity of olivine aggregates and its implications for the electrical structure of the upper mantle. Earth Planet. Sci. Lett. 288, 291–300. http://dx.doi.org/10.1016/j.epsl.2009.09.032.

Zhan, X., Schwartz, L., Toksöz, M., 2010. Pore-scale modeling of electrical and fluid transport in Berea sandstone. Geophysics 75, F135–F142. http://dx.doi.org/10.1190/1.3463704.

Zhang, B., Yoshino, T., Yamazaki, D., Manthilake, G., 2014. Electrical conductivity anisotropy in partially molten peridotite under shear deformation. Earth Planet. Sci. Lett. 405, 98–109. http://dx.doi.org/10.1016/j.epsl.2014.08.018.

Zhu, W., Gaetani, G.A., Fusseis, F., Montési, L.G.J., De Carlo, F., 2011. Microtomography of partially molten rocks: three-dimensional melt distribution in mantle peridotite. Science 332, 88–91. http://dx.doi.org/10.1126/science.1202221.